Host–guest charge transfer states: CN doped Kr and Xe

S. L. Fiedler
Department of Chemistry, University of California, Irvine, California 92697-2025

Kari Vaskonen, Jussi Ahokas, and Henrik Kunttu
Department of Chemistry, University of Jyväskylä, P.O. Box 35, FIN-40351 Jyväskylä, Finland

Jussi Eloranta
Department of Chemistry, University of California, Irvine, California 92697-2025
and Department of Chemistry, University of Jyväskylä, P.O. Box 35, FIN-40351 Jyväskylä, Finland

V. A. Apkarian[a)]
Department of Chemistry, University of California, Irvine, California 92697-2025

(Received 2 July 2002; accepted 20 August 2002)

The host–guest charge transfer absorption of CN doped krypton and xenon matrices are identified through direct analogy with the previously assigned transitions of Cl/Kr and Cl/Xe. These intense, structured absorption bands appear with the onset at 245 nm in Kr and 360 nm in Xe. Excitation of the CN/Kr charge transfer band at 193 nm leads to emission over $CN(A(^2\Pi)\rightarrow X(^2\Sigma))$ transition, indicating that an efficient curve crossing precludes the ionic state from radiating. No emissions were seen in CN/Xe when excited at 193 nm. The charge transfer absorption spectrum of CN/Kr is reproduced through an extended diatomics-in-ionic-systems treatment, using accurate *ab initio* pair potentials and transition dipoles as input, without further adjustment. The delocalized hole states are then analyzed in real-space, using atomic bases distributed over as many as eleven shells surrounding the CN^- center. The ionic states are well described as $J=1/2$, 3/2 valence bands bound to CN^-, with a substructure that cannot be exclusively assigned to a single quantum number. The strong absorptions terminate on states in which 70%–95% of the hole density remains on the first nearest neighbor shell, with hole densities of 1%–5% extended out to $R=8$ Å. In higher ionic states, with weaker transition dipoles, the hole density maximizes on shells removed by 10 Å from the ionic center. Although these delocalized states provide channels for charge separation via self-trapping of holes, save for a weak signal from the impurity trapped hole at H^+ centers, the experiments do not provide evidence for significant charge separation. © *2002 American Institute of Physics.* [DOI: 10.1063/1.1513463]

I. INTRODUCTION

Host–guest charge transfer transitions in rare gas solids (RGS), $X^-/Rg(s)^+$, represent an important class of excitations that lead to solvation dynamics peculiar to solids. Besides nuclear and electrostatic responses accompanying the sudden creation of a dipole in the polarizable dielectric medium, these transitions are accompanied by electronic solvation in the form of hole delocalization with important consequences. The prototypical systems that were first introduced for the scrutiny of such dynamics are RGS doped with halogen atoms (X=F,Cl,Br,I).[1,2,3] Among the consequences of hole delocalization are charge separation and storage in the form of self-trapped holes,[3] charge mobility, and trapping at impurity sites to create novel ionic centers such as Rg_2H^+,[4,5] and HX_2^-,[6] and reaction catalysis through charge recycling.[7] Very similar energetics is to be expected in RGS doped with the pseudohalogen, CN. This, we verify here experimentally. We identify the charge transfer transitions of CN in Kr and Xe matrices through their characteristic absorption spectra. The structure in these charge transfer absorption bands is nearly universal, as such their analysis is of significant interest. The diatomics-in-ionic-systems (DIIS) method was first introduced in the analysis of the charge transfer absorption band of Cl/Xe.[8,9] Despite the considerable success of this treatment in reproducing the absorption spectrum,[9] limiting the hole-states to the twelve nearest neighbors of the impurity precluded the possibilities of charge separation and trapping—processes that had been documented experimentally.[3] An equally satisfactory interpretation of the structure in the absorption bands could be given in terms of a Rydberg progression of hole-states pinned by the negative ion.[10] Charge separation by hole–phonon coupling and self-trapping is a natural outcome in this conceptually attractive model, which presumes an extensively delocalized hole. The solid state perspective in the analysis of these charge transfer states has been offered by Gabriel *et al.*[11] After developing the description of the band structure of rare gas solids in terms of diatomics-in-molecules (DIM),[12] they described the charge transfer states in terms of valence bands bound to a negative point charge.[11] While all three of these approaches contain common elements, an overarching picture has not yet been presented. Using CN doped Kr(*s*) as our focus, we

[a)]Author to whom correspondence should be addressed. Electronic mail: aapkaria@uci.edu

attempt a unified picture of the host–guest charge transfer states through the DIIS formalism, but now using a basis set that extends out to as many as eleven shells around the guest. This allows a real-space description of extensively delocalized states in terms of atomic bases, encompassing the molecular and band type states within the same treatment. We use input parameters obtained from high level *ab initio* calculations, and we establish the reliability of the analysis based on a detailed comparison between simulation and experiment, from finite clusters to the extended solid. With accurate input parameters, and the recognition that the DIIS approach properly accounts for quantum induction and dispersion,[13] we expect simulations of structure and energetics in many-body systems with spectral accuracy, as has already been demonstrated in the scrutiny of benchmark systems such as the HF dimer.[14] Let us remark that host–guest charge transfer transitions are not limited to halogen doped matrices. Among other documented examples are: hydrogen,[15–17] hydroxide,[18] sulfur,[19] and oxygen,[20] doped RGS. The present analysis is relevant to this general class of electronic excitations.

In what follows, in Secs. II, III, and IV we describe the experiments, the experimental findings, and the spectral assignments, respectively. The theoretical analysis is given in Sec. V, in which the DIIS construct and pair parameters is discussed. The results of the simulations and their dissection is presented in Sec. VI, followed by concluding remarks in Sec. VII.

II. EXPERIMENT

The experimental details are very similar to our previous report on HXeY (Y=Cl,Br,I,CN) species in the Xe matrix,[21] thus only a brief description is given here. The gas samples were prepared in an all glass vacuum manifold, evacuated to 2×10^{-7} mbar with a diffusion pump. Typically, guest-to-host ratios of 1:1000 were used in matrix experiments, and 30–100 mbar was deposited from 1 dm^3 volume and ~500 mbar backing pressure on a MgF_2 substrate. The substrate was cooled with a closed-cycle helium refrigerator (APD Cryogenics, Displex DE-202A); and deposition temperatures of 20 K and 30 K were used to prepare thin films of Kr and Xe, respectively.

The UV absorption spectra were recorded with a spectrometer consisting of a 30 W deuterium lamp, a 12.5-cm focal length spectrograph (Oriel Instruments, MS 125), and an image intensified charge coupled device (ICCD) camera (Andor Technologies) with 690×256 intensified pixels. The magnesium fluoride window of the deuterium lamp (Cathodeon V01) allowed access to the deep UV, down to 130 nm. Atomic lines of mercury were used for wavelength calibration of the ICCD. Laser induced fluorescence was measured with the ICCD or with a CCD camera (Princeton Instruments) mounted on a 15 cm focal length spectrograph (Acton SP150). Infrared spectra of the matrix samples were recorded with a FTIR spectrometer (Nicolet, Magna IR 760) equipped with a HgCdTe detector and a KBr beamsplitter. Photolysis of HCl and HCN was carried out with a 193 nm (ArF) excimer laser (Lambda Physik, Optex).

HCN was synthesized from an H_2SO_4: water, 1:1 solution by adding KCN to the frozen solution. Air was pumped off, and the mixture was allowed to warm up slowly. The formed gas was dried by passing it over P_2O_5, and the HCN was trapped out with liquid nitrogen and stored in a Pyrex bulb. HCl of 99.8% purity (Messer Griesheim), Kr and Xe of 99.997% purity (AGA) were obtained and used without further purification.

III. EXPERIMENTAL RESULTS

The IR spectroscopy of HCN isolated in Rg matrices has been rather thoroughly described by Abbate and Moore.[22] Spectra of HCN/Kr matrix samples deposited at 20 K mainly revealed the monomeric absorption bands of HCN. Annealing of the sample near 30 K led to limited dimerization. The monomers are identified by the characteristic pair of CH stretching frequencies, which occur at 3294.7 cm^{-1} and 3291.8 cm^{-1} in Kr, while the dimer bands are redshifted by ~100 cm^{-1}. In Xe the corresponding frequencies occur at 3279.8 cm^{-1} and 3276.4 cm^{-1}, respectively. In both cases the doublets have been ascribed to two distinct orientations of HCN in the substitutional cavity.[22] Irradiation of HCN/Kr and HCN/Xe samples at 193 nm leads to depletion of HCN absorptions, with concomitant growth of the CN radical absorptions at 2051.4 cm^{-1} and 2041.4 cm^{-1} in Kr, and at 2049.3 cm^{-1} and 2039.7 cm^{-1} in Xe.[23] In addition to CN, a weak absorption due to Xe_2H^+, at 731 cm^{-1},[24] is observed in photolyzed HCN/Xe matrices.

The UV absorption spectrum of an extensively photolyzed HCN/Kr matrix is shown in Fig. 1. The two prominent absorptions at 386 nm and 358 nm grow with photolysis. Based on the previous investigations these bands can be ascribed to the $B(^2\Sigma)\leftarrow X(^2\Sigma)$ system of the CN radical.[25,26] These absorptions possess spectral widths of ~450 cm^{-1} and their separation (2026 cm^{-1}) is comparable to what is reported in the Ne matrix.[26,27] To our knowledge, only the 0-0 transition of CN has been reported previously in Kr and Xe matrices. The very intense absorption progression, with onset near 245 nm and distinct peaks at 235 nm, 224 nm, 219 nm, and 208 nm, has not been reported previously. The similarity of this band to that of the charge transfer band of Cl doped Kr, which is provided as reference in Fig. 1, is unmistakeable. The reference spectrum was obtained by recording the absorption spectrum of a well-photolyzed HCl/Kr matrix.

As seen in Fig. 2 the situation is qualitatively very similar in Xe samples. The $0\leftarrow0$ and $1\leftarrow0$ members of the $B(^2\Sigma)\leftarrow X(^2\Sigma)$ system of the CN radical are redshifted relative to Kr, to 399 nm and 369 nm, respectively; and are broadened to ~850 cm^{-1}. The novel absorption band, which appears upon photolysis of the HCN, now extends from 350 nm to near 200 nm with maxima at 357 nm, 316 nm, 287 nm, 242 nm, and 224 nm. The analogy between this band and that of the charge transfer absorption in Cl/Xe is highlighted by the comparison in Fig. 2. The reference spectrum was obtained from a well photolyzed sample of HCl/Xe.

Laser excitation of a photolyzed HCN/Kr matrix at 193 nm yields bright fluorescence from two distinct emission systems, but no emission could be detected in Xe. One of these emission bands, illustrated in Fig. 3, can be assigned to

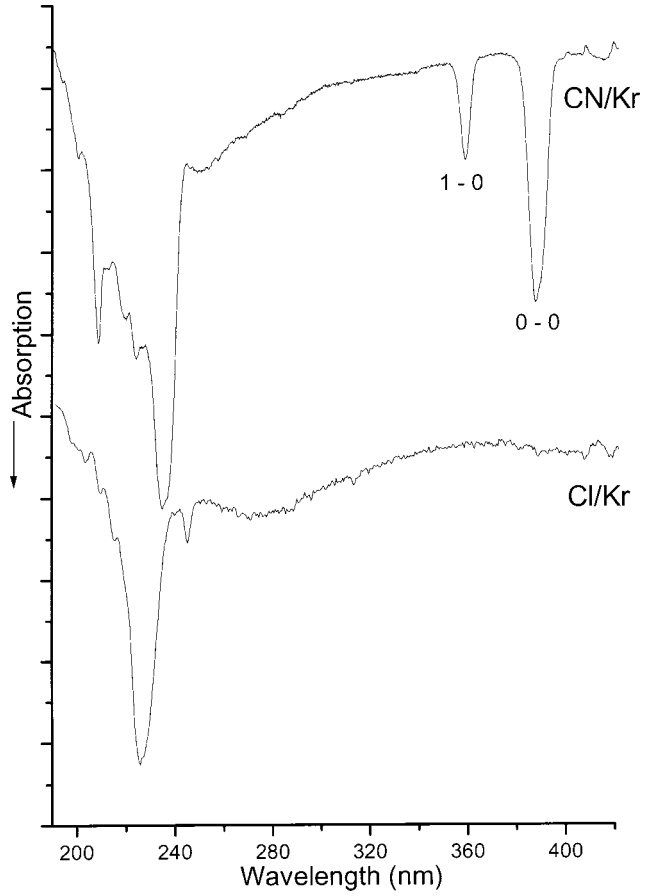

FIG. 1. UV absorption spectra of HCN/Kr and HCl/Kr matrices of 1:1000 initial guest/host ratio, after extensive irradiation at 193 nm. The peaks labeled in the upper trace are due to the $B(^2\Sigma)\leftarrow X(^2\Sigma)$ transition of the CN radical.

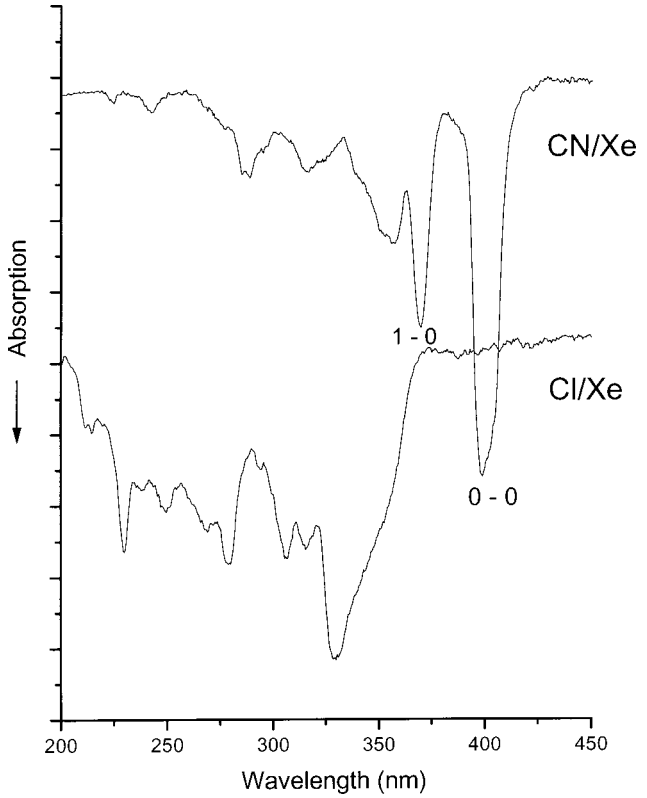

FIG. 2. UV absorption spectra of HCN/Xe and HCl/Xe matrices of 1:1000 initial guest/host ratio, after extensive irradiation at 193 nm. The peaks labeled in the upper trace are due to the $B(^2\Sigma)\leftarrow X(^2\Sigma)$ transition of the CN radical.

the $A(^2\Pi)\rightarrow X(^2\Sigma)$ vibronic progression of CN.[26–30] The $0\rightarrow 0$ band is missing from the spectrum because it lies beyond our detection sensitivity in the red. The exponential decay times of the $v'=2$ and $v'=3$ levels were measured as 120 ns and 20 ns, respectively. In Ne, the corresponding lifetimes are 670 ns and 90 ns, respectively.[27] The vibronic cascade that leads to the observation of these fluorescing states has been well analyzed and documented in Refs. 27–30. Two other emission bands are observed to grow with irradiation. The first of these occurs in the 300 nm–500 nm region, and can be identified as the Vegard–Kaplan $A(^3\Sigma_v^+)\rightarrow X(^1\Sigma_g^+)$ band of molecular nitrogen.[31] It consists of two progressions from $v'=0$ and $v'=1$ states with vibrational frequencies of 2324 cm^{-1} and 1343 cm^{-1} for the ground and excited states, and a radiative lifetime of 5.3 ms. The additional band is observed at the early stages of photolysis, and can be identified as the $C(^1\Pi_g)\rightarrow X(^1\Sigma_g^+)$ transition of C_2 in the 300–500 nm region.[25] After prolonged irradiation these lines disappeared and narrow emissions at 473 nm, 509 nm, and 553 nm, probably due to atomic carbon. The observed C_2 and N_2 may originate from dissociative charge transfer to CN trapped in special sites. We have not pursued this possibility with any systematics. Laser excitation at 248 nm did not induce any emissions in Kr.

IV. SPECTRAL ASSIGNMENTS

The spectroscopy of the CN radical isolated in Rg matrices has been rather thoroughly described in a number of previous publications.[26–30] We concentrate on the spectral region below 350 nm, which has received less attention. The electronic manifold of CN in the spectral region of the present experiment is dense. Beside the bound $A(^2\Pi)$, $B(^2\Sigma)$, and $D(^2\Sigma)$ states, a number of bound quartet states exist.[32] There are, however, strong arguments for excluding any of the valence states of the CN radical as the source for the strong absorptions seen in Figs. 1 and 2. First, the bound higher excited states are calculated to have equilibrium bond lengths comparable to the $A(^2\Pi)$ and $B(^2\Sigma)$ states,[30] and would therefore be expected to yield vibronic structure similar to the well characterized $A\leftarrow X$ and $B\leftarrow X$ absorptions. The UV absorptions shown in Figs. 1 and 2 are clearly very different from typical Franck–Condon envelopes of diatomic molecules. Second, the observed transition energies undergo a large matrix shift, characteristic of ion-pair states.[2] Thus, the strongest absorption maxima undergo a blueshift of 1.5 eV between Kr and Xe. For a typical pure molecular valence state, such as the $B(^2\Sigma)$ state of CN, the blueshift is only 0.1 eV. Third, the remarkable similarity between the spectra of Cl/Rg and CN/Rg strongly suggests that, instead of being intermolecular transitions, these strong absorptions arise from charge transfer between CN and the Rg host. This is further confirmed by considering the relative shifts between CN/Rg and Cl/Rg. Given the similarity of sizes between

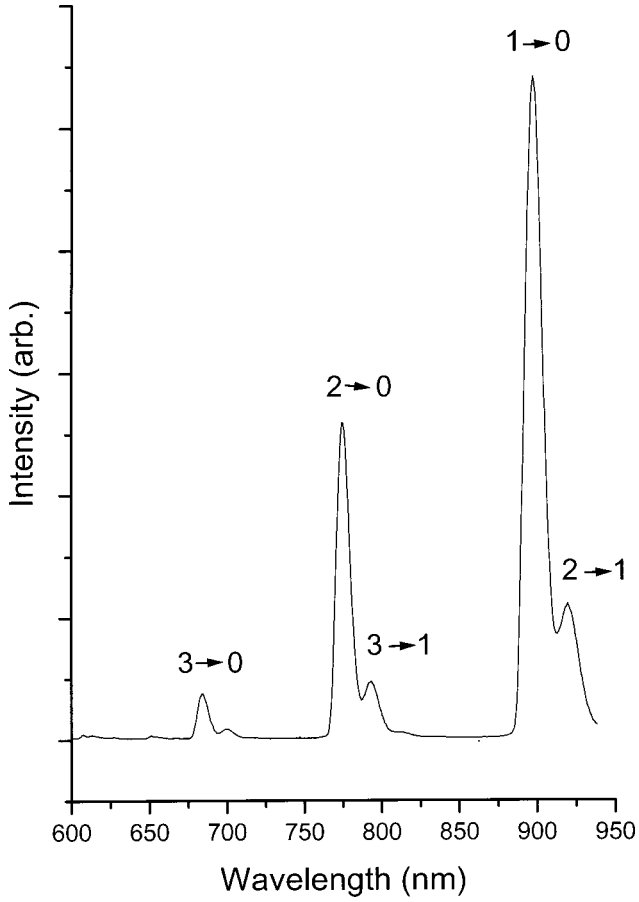

FIG. 3. Portion of the $A(^2\Pi)\rightarrow X(^2\Sigma)$ emission spectrum in a HCN/Kr matrix after extensive irradiation at 193 nm.

CN^- and Cl^-, we would expect the shift between their charge transfer bands within a given RGS to scale by their electron affinities. In the Kr matrix the main maxima of CN and Cl are located at 234 nm and 224 nm yielding a redshift of 0.23 eV, which is very close to the difference in the electron affinities of 0.25 eV (electron affinities of CN and Cl are 3.86 eV and 3.61 eV, respectively).[33,34] Although the band origins are less well defined in Xe, comparison of the first maxima at 357 nm for CN and at 330 nm for Cl yields a rather consistent value for the relative shift of 0.19 eV. To a first approximation, the host dependence of the host–guest charge transfer energy may be ascribed to the difference in ionization energies of the host atoms. Consistent with this expectation, the experimental matrix shifts for Cl and CN absorption origins are 1.77 eV and 1.83 eV, respectively, compare well with the 2 eV difference in ionization potentials of Kr and Xe.

The above arguments overwhelmingly establish the origin of the UV absorption bands to charge transfer transitions of CN/Rg(*s*). The similarity of these excitations to the corresponding halogen doped solids is limited to the absorption bands only. The relaxation pathways subsequent to absorption are quite different. As a general rule, the charge transfer states of halogen doped matrices relax to form the localized triatomic exciplexes, $Rg_2^+X^-$, which then relax radiatively with 100% quantum efficiency.[2,35] In contrast, in CN/Kr the charge transfer absorption leads to strong emission over the $CN(A\rightarrow X)$ transition, after some 5 eV of nonradiative decay. Quite clearly, efficient crossing to the internal vibronic states of the molecular guest occurs with subsequent cascade among the nested *B* and *A* potentials of the radical. This channel of relaxation may also compete with the possibilities of charge separation from the ionic state, as is known to happen in the halogen doped solids.[3] Indeed, we have unsuccessfully searched for CN^- through IR spectroscopy. As mentioned in the Results, we do observe the IR absorption due to Xe_2H^+, which would in principle signify the presence of CN^- as a counterion. However, we should note that water impurities in Xe are known to yield the hydrogen ion upon 193 nm irradiation. Barring this source, we must conclude that either the CN^- absorptions are too weak to observe, or that they undergo efficient charge recombination in the excited state (as evidenced by the neutral CN fluorescence) or in the ground state assisted by photoionization of the CN^- centers during irradiation.

V. THEORETICAL METHOD AND PARAMETERS

A. The DIIS construct

The present theoretical treatment of the host–guest charge transfer states is rooted in the original DIIS construct, which was designed to properly account for many body induction terms.[8] The important differences are: the use of significantly extended hole bases distributed over as many as eleven shells surrounding the guest site; and the use of input parameters, potentials, and transition dipoles, obtained from high level *ab initio* calculations; and a precise treatment of the transition dipole in the extended system. Beside simulating the spectra, we use the analysis to extract descriptions of the observables and their underlying structure and energetics.

The polyatomic basis functions that represent the system are constructed according to the DIM, from atomic bases subject to the zero-overlap assumption.[36–38] The neutral ground state consists of the open shell $CN(X\,^2\Sigma)$ and closed shell $Kr(^1S)$ atoms,

$$CN(X\,^2\Sigma)Kr_0(^1S)Kr_1(^1S)Kr_2(^1S)\ldots . \tag{1a}$$

The excited charge transfer states consist of the closed shell CN^- ion, and a single *p*-hole placed on one of the Kr atoms,

$$CN^-(^1S)Kr_0^+(^2P)Kr_1(^1S)Kr_2(^1S)\ldots,$$

$$CN^-(^1S)Kr_0(^1S)Kr_1^+(^2P)Kr_2(^1S)\ldots,$$

$$CN^-(^1S)Kr_0(^1S)Kr_1(^1S)Kr_2^+(^2P),\ldots . \tag{1b}$$

The system Hamiltonian then consists of the neutral, ground state block, and the excited, ionic block,

$$\mathbf{H}=\mathbf{H}^{(g)}\oplus\mathbf{H}^{(i)}. \tag{2}$$

Throughout the treatment we will neglect the anisotropy of Kr–CN versus Kr–NC, as well as the spin–orbit splitting in CN. Accordingly, the ground state Hamiltonian is limited to

three dimensions, determined by the three Cartesian orientations of the CN radical in the laboratory frame. In the molecular CN–Kr frame, this reduces to parallel and perpendicular components, Σ and Π, and is explicitly evaluated as

$$\mathbf{H}^{(g)}=\sum_i \mathbf{R}^{-1}(\theta,\phi) \times\begin{vmatrix} V_g^{\Pi}(\mathrm{Kr}_i\mathrm{CN}) & 0 & 0 \\ 0 & V_g^{\Pi}(\mathrm{Kr}_i\mathrm{CN}) & 0 \\ 0 & 0 & V_g^{\Sigma}(\mathrm{Kr}_i\mathrm{CN}) \end{vmatrix} \times\mathbf{R}(\theta,\phi)+\left[\sum_i \sum_{j>i} V(\mathrm{Kr}_i\mathrm{Kr}_j)\right]\otimes\mathbf{I}. \tag{3}$$

$\mathbf{R}(\theta,\phi)$ is the direction cosine matrix that rotates the CN principle axis toward the ith Kr atom. Inclusion of spin–orbit coupling expands the rank of $\mathbf{H}^{(g)}$ from 3 to 6.

In the absence of spin–orbit splitting, the uncoupled p-hole bases are threefold degenerate, p_x, p_y, p_z. Therefore the ionic block $\mathbf{H}^{(i)}$, indexed by the atom on which the p-hole occurs, consists of three-dimensional diagonal matrices $\mathbf{V}(\mathrm{CN}^- - \mathrm{Kr}_i)$ and off-diagonal exchange matrices $\mathbf{J}_{i,j}$, given as

$$\mathbf{J}_{i,j}=\begin{vmatrix} J^{\Pi}(\mathrm{Kr}_i\mathrm{Kr}_j)^+ & & \\ & J^{\Pi}(\mathrm{Kr}_i\mathrm{Kr}_j)^+ & \\ & & J^{\Sigma}(\mathrm{Kr}_i\mathrm{Kr}_j)^+ \end{vmatrix} \tag{4a}$$

with fragment exchange energies given in the diatomic frame,

$$J^{\Sigma}=[V(\Sigma_u)-V(\Sigma_g)]/2 \quad \text{and} \quad J^{\Pi}=[V(\Pi_u)-V(\Pi_g)]/2. \tag{4b}$$

Once again, direction cosine matrices are used to rotate the Kr^+ p-hole from the laboratory frame toward the molecular $\mathrm{Kr}_j-\mathrm{Kr}_i$ direction.

The diagonal elements of the ionic block are evaluated following the DIIS strategy, which recognizes that induction energies cannot be decomposed into pairwise additive terms.[8] Induction energies are determined as the polarization of a given neutral Kr by the net field it experiences for a given choice of Kr^+ and CN^- centers. To account for dielectric screening, it is economical to evaluate the field due to a single charge by the self-consistent electrostatic expansion in a discrete lattice,[39] to extract an effective screening constant ε through fitting,

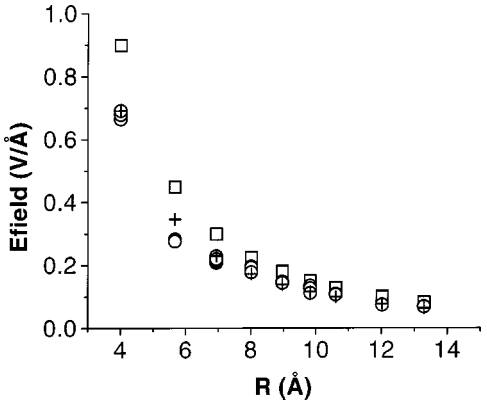

FIG. 4. The self-consistent electric field due to a substitutional charge at the origin of a perfect Kr lattice. The bare ion field, self-consistent field, and a screened electric field $\varepsilon=1.3$, are represented as solid squares, open circles, and crosses, respectively.

$$\mathbf{E}(r)=\frac{q\mathbf{r}}{\varepsilon r^3}. \tag{5}$$

This is shown for the case of Kr in Fig. 4. A dielectric constant of $\varepsilon=1.3$ fits the data. The net induced ion–dipole energy, W_i, on the ith Kr atom by the CN^- and Kr^+ ion pair is then given as

$$W=\frac{\alpha}{2}(\mathbf{E}^+ + \mathbf{E}^-)^2. \tag{6}$$

To implement this, we decompose the ionic pair potentials in terms of valence, induction and dispersion contributions by fitting the $\mathrm{Kr}^+\mathrm{Kr}$ and $\mathrm{CN}^-\mathrm{Kr}$ pair potentials to the Rittner form.[40] The pairwise additive part of ionic interactions is then obtained by subtracting the charge induced dipole contribution, e.g.,

$$\tilde{V}^{\Sigma}_{\mathrm{Kr}^+\mathrm{Kr}^-}(R)=\frac{V^{\Sigma_u}(R)+V^{\Sigma_g}(R)}{2}+\frac{C_4}{R^4}. \tag{7}$$

The three-center induction energies are then added separately (charge induced quadrupole and higher pole terms are not distinguished from the dispersion terms). The diagonal blocks of $\mathbf{H}^{(i)}$ are explicitly given as

$$\mathbf{V}^{(i)}=\mathbf{R}^{-1}\begin{vmatrix} V^{\Pi}(\mathrm{CN}^-\mathrm{Kr}_i^+) & 0 & 0 \\ 0 & V^{\Pi}(\mathrm{CN}^-\mathrm{Kr}_i^+) & 0 \\ 0 & 0 & V^{\Sigma}(\mathrm{CN}^-\mathrm{Kr}_i^+) \end{vmatrix}\mathbf{R}+\sum_j \mathbf{R}^{-1}\begin{bmatrix} \tilde{V}^{\Pi}(\mathrm{Kr}_i^+\mathrm{Kr}_j) & 0 & 0 \\ 0 & \tilde{V}^{\Pi}(\mathrm{Kr}_i^+\mathrm{Kr}_j) & 0 \\ 0 & 0 & \tilde{V}^{\Sigma}(\mathrm{Kr}_i^+\mathrm{Kr}_j) \end{bmatrix}\mathbf{R} + \left(\sum_j \tilde{V}(\mathrm{CN}^-\mathrm{Kr}_j)+\sum_{j\neq i}\sum_{k>j} V(\mathrm{Kr}_j\mathrm{Kr}_k)+W_i+W_{\mathrm{cavity}}+\mathrm{IP}-\mathrm{EA}\right)\otimes\mathbf{I}, \tag{8}$$

in which W_i is the total ion-induced dipole energy, and W_{cavity} is the Onsager polarization energy of the dielectric outside the cavity in which the explicit evaluation of induction is carried out;[41] IP is the ionization potential of Kr and EA is the CN electron affinity.

Spin–orbit coupling in Kr^+ cannot be ignored. It is incorporated via the atoms-in-molecules approach developed by Mies,[42] which has been employed frequently in DIM calculations. The total Hamiltonian is now given as

$$\mathbf{H}_{\text{Total}} = \mathbf{H}_{\text{el}} + \mathbf{H}_{\text{so}} = \mathbf{H}_{\text{el}} + \Delta \hat{\mathbf{l}} \cdot \hat{\mathbf{s}} \tag{9}$$

in which $\Delta = 0.67$ eV, is the Kr^+ spin–orbit splitting. The polyatomic base functions now expand by a factor of 2, by the addition of $m_s = \pm 1/2$ labels. To evaluate $\mathbf{H}_{\text{so}}$, which is diagonal in the jm_j coupled basis, the uncoupled Hamiltonian is transformed using the standard coupling matrices of Clebsch–Gordan coefficients.

The transition dipole moments were calculated in a pairwise additive approach, initially resembling the full DIM method described by Naumkin[43] and Gadea and Amarouche[44] for the Rg ion clusters. The transition dipole in the KrCN molecular frame can be expressed as

$$\boldsymbol{\mu}_{M,if} = \langle f | \mathbf{R}_{LM}^{-1} \boldsymbol{\mu}_M \mathbf{R}_{LM} | i \rangle \tag{10}$$

in which $\mathbf{R}_{LM}$ rotates initial and final state eigenvectors from the laboratory to the molecular frame, for a hole localized on a particular Kr atom. The nonzero elements in the transition dipole matrices can be found by symmetry.[45] Since in the ionic states of interest, the hole is delocalized among many Kr atoms, the net transition dipole for a particular final state is found by rotating the molecular transition dipole vectors to the laboratory frame, then summing over the pairs,

$$\boldsymbol{\mu}_L = \sum_j R_{LM}^{-1} \boldsymbol{\mu}_{M,j} \tag{11}$$

in which L and M indices refer to laboratory and molecular frames, respectively.

B. Fragment energetics

The diatomic fragment energies, required as input parameters to evaluate the above DIIS matrices consist of the pair potentials of Kr_2, $Kr_2^+(\Sigma_g, \Sigma_u, \Pi_g, \Pi_u)$, $KrCN^-$, $Kr^+CN^-(\Sigma, \Pi)$, and KrCN. These potentials are collected in Figs. 5 and 7. Both linear Kr–CN and Kr–NC geometries and the "T" geometry were computed, however, the orientationally averaged potential is used in the simulations.[46] This is done with the knowledge that in the tight substitutional site of both solid Kr and Xe, the CN radical undergoes free rotation.[29,47] In effect, the pair potential anisotropy is lifted by the compact site, by averaging over the twelve nearest neighbors. To simulate the angular isotropy imposed by the $N = 0$ state, to which the radical must be limited at the cryogenic temperatures of relevance, we use the rotationally averaged pair potential. However, to evaluate transition dipoles, the Σ and Π distinctions (linear and "T" orientation) in the ground electronic state must be maintained to properly account for the significant differences in $\Sigma \leftrightarrow \Sigma$, $\Pi \leftrightarrow \Pi$, and $\Sigma \leftrightarrow \Pi$ transitions that occur on the molecular CN–Kr reference frame.

The neutral Kr–Kr interactions are represented through the Aziz potentials.[48]

The ground state $CN(^2\Sigma) - Kr(^1S)$ interaction (linear geometries in C_{2v} symmetry) were first obtained at the restricted Hartree–Fock (RHF) level, which was then used as a reference state for subsequent spin unrestricted coupled cluster with single, double, and perturbative triples substitutions (UCCSD(T)) calculation.[49] For the CN fragment, Dunning's augmented correlation consistent basis set aug-cc-pVQZ (AVQZ) (Ref. 50) was used, whereas the effective core potential (ECP) basis set of the Stuttgart group[51] was applied for Kr. Since the calculation is based on a single reference, the validity of this assumption has to be verified. The standard test, i.e., the norm of the single excitation vector, was calculated to be below 0.05.[52] This indicates that the contribution of single excitations is minor and thus UCCSD(T) can be expected to yield very reliable results. Because binding on the ground state is weak and caused by the van der Waals interaction it is essential to correct the obtained potential energy curves for basis set superposition errors (BSSE). In the present work we have applied standard counterpoise correction procedure by Boys and Bernardi, which relies on the size-consistency of the coupled cluster method.[53]

The CCSD(T) method is applicable only for the lowest state of a given symmetry, thus another approach is needed for treating the ionic states of interest. First the initial reference state is obtained from a RHF calculation for the ground state, and followed by state averaged multiconfiguration self-consistent field (MCSCF) calculation utilizing complete active space (CAS) orbitals.[54] Orbitals involving the $X\,^2\Sigma$, $A\,^2\Pi$, and $B\,^2\Sigma$ molecular states of CN and the outer p-orbitals of Kr were included in the active space. In this computation, all six states were calculated simultaneously via state averaging. Inclusion of A and B states of CN is essential in order to obtain proper convergence to the ionic states in a subsequent multireference configuration interac-

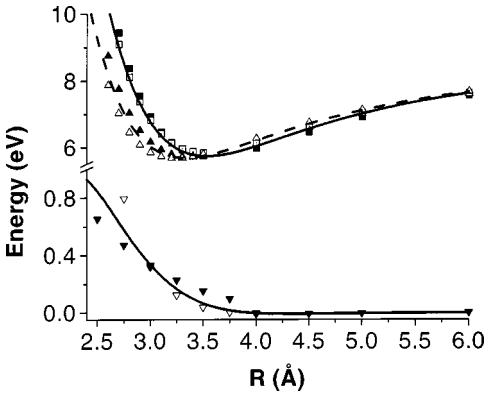

FIG. 5. The *ab initio* KrCN and Kr^+CN^- pair potentials (see text for details). In the implementation, the mean over the Kr–CN and Kr–NC orientations is used: Solid squares, $Kr^+NC^-(\Sigma)$; solid up triangles, $Kr^+NC^-(\Pi)$; open squares, $Kr^+CN^-(\Sigma)$; open up-triangles, $Kr^+CN^-(\Pi)$; upper solid line, $Kr^+CN^-(\Sigma)$ fit; dashed line, $Kr^+CN^-(\Pi)$ fit; open down-triangle, NCKr; solid down-triangle, CNKr; lower solid line, CNKr(X) fit to mean.

tion (MRCI) calculation. As mentioned, after the MCSCF calculation internally contracted MRCI calculation with single and double excitations was carried out in order to account for electron correlation to proper extent.[55] All quoted energies were subject to the multireference analog of the Davidson correction.[56] The spin–orbit matrix elements were evaluated by the spin–orbit pseudopotential method, with parametrization present in the Stuttgart ECP basis, using IC-MRCI wave functions.[57] The spin Hamiltonian matrix of the spin–orbit operator was constructed in the basis of the non-relativistic Hamiltonian and diagonalized to yield the spin–orbit eigenstates. The present calculations yield correct asymptotic energetics for all six states, including spin–orbit splitting of Kr^+. The transition dipole moments between the spin–orbit split states were calculated using wave functions obtained from diagonalization of the spin Hamiltonian. The MRCI calculations employed the same basis set as the coupled clusters calculations described above. All CCSD(T) and MRCI calculations were carried out with the MOLPRO 2000.1 software package on GNU/LINUX platforms.[58]

The linear KrCN and KrNC pair potentials are shown in Fig. 5, along with the mean of these two geometries. Note, the minimum in this pair interaction occurs at 4.5 Å, to be compared to the nearest neighbor distance in solid Kr of 3.99 Å. Accordingly, the CN radical would be expected to fit in a somewhat expanded substitutional site of the lattice. The tight-fit among 12 octahedrally situated nearest neighbors lifts the angular anisotropy of the CN–Kr interaction. The Kr^+CN^- potentials are also shown in Fig. 5. The potential minima of the ion-pair states occur at 3.53 Å and 3.33 Å in the Σ and Π states, respectively, at significantly smaller distances than in the neutral ground state. We may therefore expect contraction of the lattice site upon charge transfer excitation. This has been recognized experimentally in halogen doped matrices, through the indirect observation of transient self-focusing.[59] The transition dipoles associated with charge transfer transitions are determined by the overlap between the valence electron function in the initial state and the hole wave function in the final state. As such, the main contribution to absorption arises from $\Sigma \rightarrow \Sigma$ transitions, with nearly an order of magnitude smaller contribution from $\Sigma \rightarrow \Pi$ and $\Pi \rightarrow \Pi$ transitions. The orientationally averaged, Kr–CN/Kr–NC, computed transitions dipoles are shown in Fig. 6. In the range $r > 3$ Å, the transition dipoles are well fit by the functions,

$$\mu_{\Sigma-\Sigma}(r) = 18 \exp[-(r-0.82662)/1.07365], \tag{12a}$$

$$\mu_{\Sigma-\Pi}(r) = 5.535\,89 \exp[-(r+0.49169)/0.93593]. \tag{12b}$$

We ignore the $\Pi \rightarrow \Pi$ transitions entirely; and although we include the $\Sigma \rightarrow \Pi$ transitions, we have verified that their neglect has little effect on the final spectra. The orientationally averaged, computed $KrCN^-$ potential is well represented by the function,

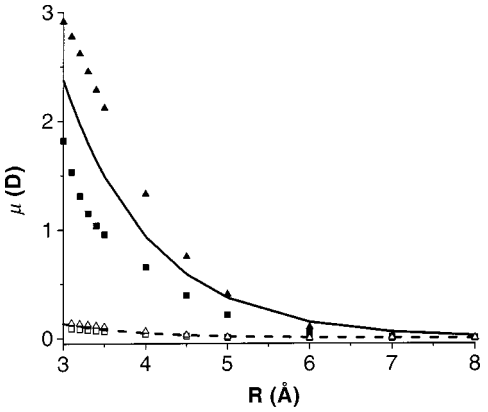

FIG. 6. The distance dependence of the transition dipole moment for the $Kr^+CN^- \leftarrow KrCN$ charge transfer absorption: CNKr $\Sigma \leftarrow \Sigma$ (solid squares), NCKr $\Sigma \leftarrow \Sigma$ (solid triangles), CNKr $\Sigma \leftarrow \Pi$ (open squares), NCKr $\Sigma \leftarrow \Pi$ (open triangles), $\Sigma \leftarrow \Sigma$ fit (solid line) and $\Sigma \leftarrow \Pi$ fit (dotted line).

$$V_{KrCN^-}(r) = 1290 \exp[-(r+1.41)^2/2.80] - \frac{17.76}{r^4} - \frac{148}{r^6}, \quad \text{for } r > 3.3 \text{ Å}. \tag{13}$$

The Kr_2^+ potentials were calculated via the coupled clusters approach (MOLPRO) using the aug-cc-pV5Z basis. The resulting curves are shown in Fig. 7. The adiabatic ionization energies of Kr_2 have recently been measured using zero-kinetic energy photoelectron spectroscopy (ZEKE). The lowest adiabatic ionization limit of the dimer, terminating on the $Kr_2^+(I1/2_u)$ state, is found to be $103\,773.6 \pm 2\ cm^{-1}$.[60] The calculated value for the same in the present approach is $103\,756\ cm^{-1}$, therefore in excellent agreement with the best known experimental value. This gives good confidence for the entire curve, the asymptote of which is also exactly known and incorporated. The Kr_2^+ potentials were explicitly calculated for $R < 5.3$ Å, and splined to the curves calculated analytically for $R > 6.3$ Å as induction (charge induced dipole) and dispersion (R^{-6}) using the polarizability of Kr as the sole input. As a test of the accuracy of the excited Kr_2^+ potentials, we have simulated the known absorption bands of the dimer ion.[61,62] The spectral profiles are reproduced within the experimental uncertainty of these systems. As a more

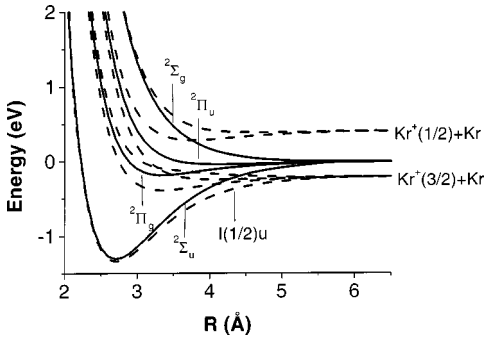

FIG. 7. The computed Kr_2^+ pair potentials. The potentials without spin–orbit coupling (solid) were calculated using the coupled clusters method (see text). The potentials with spin–orbit coupling (dashed) are obtained by assuming a distance independent coupling constant.

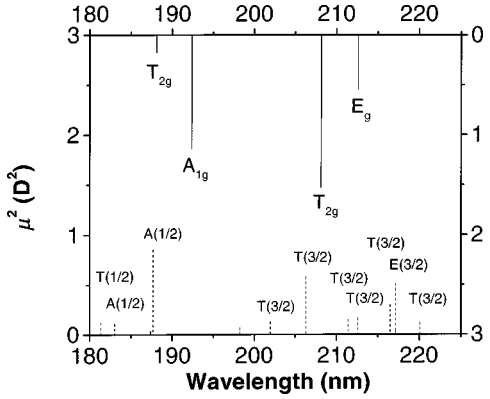

FIG. 8. The absorption stick spectrum of $Kr_{12}CN$ with (lower set, left abscissa) and without (upper set, right abscissa) spin–orbit coupling. The effect of spin–orbit coupling is to mix the four bright states with otherwise dark states, while preserving the oscillator strength (squared magnitude of the transition dipole, $\langle\mu\rangle^2$) under each set of mixed states. The structure of the cluster is fixed with the 12 Kr atoms occupying the lattice points of the perfect, fcc Kr lattice.

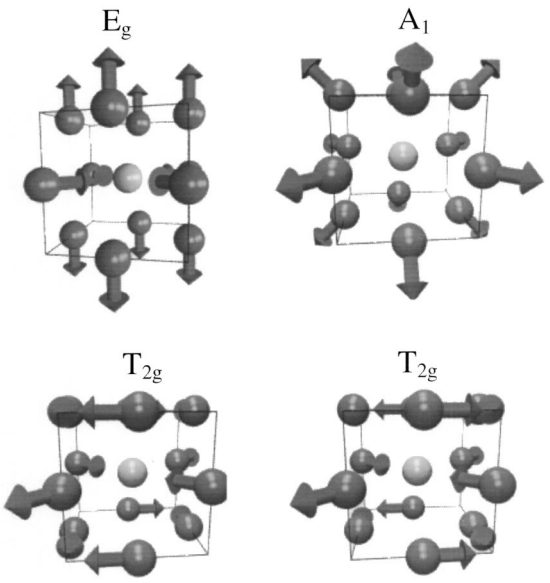

FIG. 9. The eigenvectors of the dipole allowed ionic states, identifying the orientations and magnitudes of the *p*-holes distributed on the Kr atoms.

rigorous test of the construct,[63] we have verified that the same potentials also reproduce the known absorption spectra of Kr_3^+.[64]

VI. THEORETICAL RESULTS

A. $Kr_{12}CN$

We first consider the finite cluster of CN surrounded by 12 Kr atoms, in an octahedral arrangement mimicking the substitutional site of a perfect fcc lattice. In the absence of spin–orbit coupling, the *p*-hole can occur in any one of the three possible Cartesian directions on each of the 12 Kr atoms, to produce a basis set of 36 ionic states. Due to the high symmetry of the cluster, only four of the 36 states carry significant transition dipole. The symmetries of the bright states can be identified from the eigenvectors. In order of energy, they belong to the E_g, T_{2g}, A_{1g}, and T_{2g} irreducible representations of O_h as shown in Fig. 8. The $^2\Pi$ ground state belongs to the T_{1u} representation.

The inclusion of spin–orbit coupling expands the ionic manifold to 72 states (each a Kramers' pair). The parentage of these states is identified by gradually turning on the spin–orbit Hamiltonian, which was done to obtain the correct state labels shown in Fig. 8. As the spin–orbit interaction is turned on, many of the dark states borrow intensity by mixing through the $\mathbf{l}\cdot\mathbf{s}$ Hamiltonian. The net oscillator strength, sum of $\langle\mu\rangle^2$ over all allowed transitions is conserved; moreover, the oscillator strength within a correlated set of states remains conserved. This is perhaps clearest for the A_{1g} state, which correlates with two $J=1/2$ states. Figure 8 also illustrates the separation of the spin–orbit coupled states into the $J=3/2$ and $J=1/2$ groups. However, within the $J=3/2$ manifold, the $\Omega=1/2$ and 3/2 projections remain mixed.

The spatial distribution of the delocalized hole states can be clearly visualized by considering the eigenvectors. The four optically allowed charge transfer states in the $L-S$ coupling limit are illustrated in Fig. 9. Beside the irreducible representations of the O_h group to which these states belong, they are identified by state numbers in ascending order of eigenenergies. The vector directions, which are shown with perspective to visualize the three-dimensional direct space charge distributions, identify the orientation (phase) of the *p*-hole on a given atom, while the length of a given vector represents the atomic charge density. In the totally symmetric A_{1g} state, the *p*-holes point radially out of the CN^- center. Therefore, the polyatomic function in this state can be identified as an *S*-wave (*S*-hole). All other states belong to degenerate representations, for which we only show one of the possible real components. The shown component of the E_g state, can be identified collectively as a d_{z^2} function, therefore a *D*-hole. The identification of the collective T_{2g} hole-states are less direct from the visualization, however, these states will correlate with the d_{xy}-type orbitals in O_h symmetry. In effect, in the uncoupled representation, the optical transitions can be identified as $\Delta L=\pm 1$ hole transitions: $S(A_{1g})\leftarrow P(T_{1u})$ and $D(E_g,T_{2g})\leftarrow P(T_{1u})$, where L refers to the angular momentum of the collective hole state. Note, upon inclusion of spin–orbit coupling, the lowest state of the ionic manifold, $T_{2g}(3/2)$ becomes dipole allowed by borrowing intensity.

To incorporate the zero-point vibrational distribution of the ground state, we carry out Monte Carlo simulations at an effective temperature that reproduces the zero-point amplitude of the Kr–CN pair (classical $T=21$ K). The resulting spectrum is compared with the stick spectrum of the perfect cube in Fig. 10. Although all features undergo a blueshift, the parentage of the broadened spectral features of the structurally relaxed cluster is clear. The origin of the blueshift can be understood on the basis of the pair potentials. Since the CN–Kr internuclear minimum, which occurs at 4.5 Å,[48] is larger than the nearest neighbor distance of 4 Å in solid Kr, the cube expands. Since the vertical transition in the pair interaction leads to the attractive branch of the Kr^+CN^- potential (see Fig. 5), the expansion of the site necessarily leads to an increase in transition energy (blueshift). Also, the Monte Carlo sampling of the vibrational distribution breaks

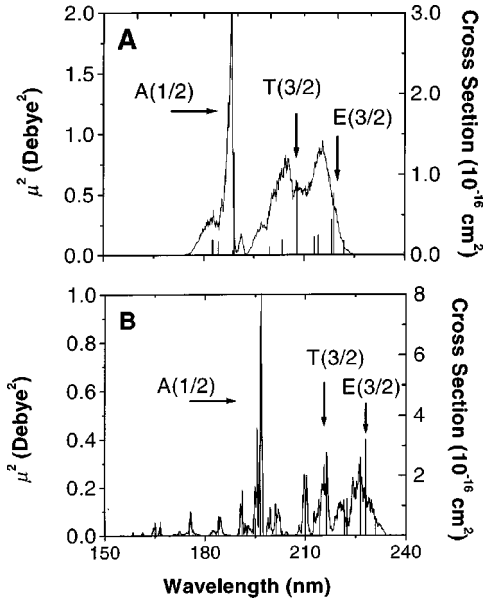

FIG. 10. Stick spectrum of the perfect rigid cluster, vs vibrationally averaged spectrum of the structurally relaxed cluster: (a) $Kr_{12}CN$, (b) $Kr_{42}CN$. Monte Carlo sampling of the ground state vibrational amplitude is implemented, using an effective temperature of 18 K that reproduces the vibrational zero-point amplitude of the Kr–CN pair.

the perfect cubic symmetry of the cluster, increasing the number of optically allowed transitions. The comparison in Fig. 10 shows that, at least at 0 K, vibrationally activated optical transitions do not materially change the spectrum.

B. $Kr_{42}CN$

The simulated spectrum of $Kr_{42}CN$, with Monte Carlo sampling of the initial state vibrational distribution at 0 K is shown in Fig. 11, along with the stick spectrum of the perfect cluster. This cluster contains three complete shells of Kr atoms. Although a larger number of states are now optically active, the state assignments and their spectral distribution follows the same pattern as in the $Kr_{12}CN$. In this case, the

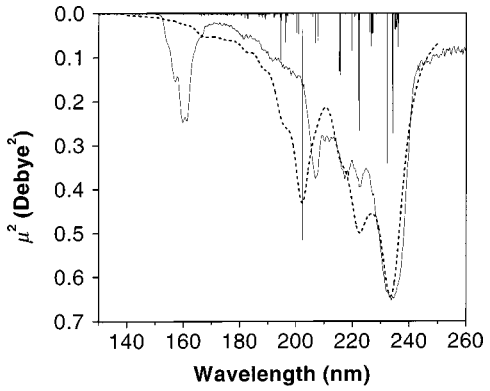

FIG. 11. Simulated spectra of the CN/Kr charge transfer absorption in the extended solid. The simulations use a hole basis set distributed aver the first eleven complete shells (224 atoms) around the substitutionally trapped CN radical. The stick spectrum is for the relaxed configuration in the neutral ground state, reached by simulated annealing. The smoothed simulated spectrum is obtained by replacing the spectral lines with Lorentzians of FWHM=0.2 eV.

spectrum of the structurally relaxed cluster essentially provides contouring around the stick spectrum, without a significant spectral shift. The blue shift due to structural relaxation observed in the $Kr_{12}CN$ cluster is compensated by the fact that the first shell now expands against the outer Kr shells. The inter-shell compression leads to a deeper part in the Kr_2^+ potential. As before, vibrationally activated optical transitions make a negligible contribution to the overall shape of the simulated spectrum. In effect, the Monte Carlo simulation can be well approximated by adding widths to the stick spectrum. In both the $Kr_{12}CN$ and the $Kr_{42}CN$ spectra the strongest transition is to the $J=1/2$, $\Omega=1/2$, or the *S*-hole state, which shifts from 185 nm to 195 nm as the cluster size grows. To the red of this line are the charge transfer transitions involving the $J=3/2$ hole. These transitions clump together to generate structure in the spectra smoothed by vibrational sampling in the initial state. As indicated in the spectra, the structure can be traced to crystal field split T_{2g} and E_g components, by progressively switching the spin–orbit coupling off. However, the states in the different absorption bands are strongly contaminated by spin–orbit mixing, which can be concluded by finding that the projection of the angular momentum in the collective hole state, $\Omega=\Sigma_i m_{l_i}$, where the summation is over the atomic *p*-holes in the uncoupled representation, is ill-defined. Similarly, the projection of the total angular momentum in the coupled basis set remains ill-defined, and therefore the substructure cannot be assigned to the $\Omega=3/2$ and 1/2 components of the $J=3/2$ hole, which in the valence band would be identified as the heavy hole and light hole.[65] The strong Coulombic binding of the hole to the impurity leads to strong mixing between these two branches of the valence band. Although this observation is based on the finite size cluster, the same holds in the extended solid treatment, which we consider next.

C. The extended solid

We approximate the solid state spectrum by distributing 224 base atoms, namely, by allowing the *p*-hole to be distributed over 11 complete shells around a central CN. The rest of the infinite solid is simply accounted for by assuming a continuum dielectric around the spherical cluster. Converged statistical simulations, such as the Monte Carlo simulations used in the smaller clusters, become prohibitive in this basis set since diagonalization of 1350×1350 matrices is required for each configuration (eigenvectors of length $224\times6+6$). However, simulations of the smaller clusters give us confidence that despite the undersampled statistics, realistic 0 K spectra can be expected by inclusion of line profiles. We carry out the simulations on the structurally relaxed, minimum energy configuration of the $Kr_{224}CN$ cluster, which is obtained by simulated annealing on the ground electronic state. The stick spectrum of the annealed structure is compared with the experiment in Fig. 11. The simulated lines are in good registry with the experimental structure. The exception is the 160 nm band seen in the experiment, which is absent in the simulation. This discrepancy we take to indicate that the 160 nm absorption is not part of the charge transfer

TABLE I. Description of selected, optically active charge transfer states of the extended solid.

State	22	26	34	50	64	84	95	122	131	179	194	221	271
λ (nm)	232.19	227.21	222.50	215.34	202.35	196.37	194.56	189.02	188.03	183.96	182.62	181.08	178.15
$\lvert\langle\mu\rangle\rvert^2$	0.3411	0.0439	0.2665	0.1313	0.5152	0.0016	0.1059	0.0129	0.0301	0.0004	0.0046	0.0001	0.0026
$\langle Q\rangle$	−3.9271	−3.8347	−3.8440	−3.7347	−3.5042	−2.6557	−2.4938	−2.0215	−2.1021	−1.8374	−1.8322	−1.7068	−1.7249
$\langle J\rangle$	−0.3456	−0.3639	−0.2462	−0.1691	−0.2411	−0.3997	−0.3798	−0.4592	−0.3954	−0.4017	−0.4060	−0.4089	−0.3676
Shell No.	R (Å)	Charge per shell											
1	4.02	0.9484	0.9269	0.8901	0.8519	0.6764	0.2240	0.1150	0.0197	0.0436	0.0112	0.0132	0.0173	0.0061
2	5.59	0.0012	0.0291	0.0565	0.0825	0.1893	0.3020	0.3649	0.0693	0.0505	0.0229	0.0557	0.0220	0.0546
3	6.85	0.0333	0.0372	0.0332	0.0510	0.0653	0.3832	0.3903	0.4575	0.5829	0.2918	0.2186	0.1229	0.1538
4	7.91	0.0156	0.0048	0.0160	0.0101	0.0445	0.0147	0.0314	0.2412	0.1107	0.1514	0.1786	0.1016	0.1265
5	8.83	0.0003	0.0012	0.0028	0.0028	0.0159	0.0416	0.0700	0.1408	0.1355	0.4043	0.3709	0.4224	0.3108
6	9.66	0.0002	0.0001	0.0002	0.0002	0.0019	0.0174	0.0114	0.0176	0.0328	0.0100	0.0150	0.0673	0.0759
7	10.46	0.0009	0.0007	0.0008	0.0013	0.0053	0.0148	0.0133	0.0425	0.0354	0.0868	0.1060	0.1944	0.1970
8	11.19	0.0000	0.0000	0.0000	0.0000	0.0000	0.0001	0.0005	0.0032	0.0011	0.0031	0.0152	0.0062	0.0100
9	11.88	0.0002	0.0001	0.0002	0.0002	0.0012	0.0008	0.0017	0.0052	0.0041	0.0133	0.0184	0.0290	0.0454
10	12.53	0.0000	0.0000	0.0000	0.0000	0.0003	0.0007	0.0012	0.0018	0.0021	0.0032	0.0047	0.0118	0.0117
11	13.10	0.0000	0.0000	0.0000	0.0000	0.0001	0.0007	0.0005	0.0012	0.0015	0.0021	0.0036	0.0052	0.0084

transition. The remaining spectrum can be well reproduced by assuming Lorentzians for the spectral lines, as shown in Fig. 11. The resulting spectrum is an unmistakable reproduction of the experiment. Most features of the experiment are quantitatively reproduced, although there is a ~5 nm shift in the position of the $S_{1/2}$-hole absorption at 200 nm.

The dressing of the line spectrum with Lorentzians can be justified by recognizing that beside the thermal vibrational distribution in the ground electronic state, the absorption lines will be dynamically broadened by electronic dephasing. The latter is a measure of the strength of hole–phonon coupling. The assumed Lorentzian widths were 0.2 eV (FWHM), which if strictly interpreted as arising from electronic dephasing, would imply a decay time of ~7 fs. This very short time, much shorter than any vibrational motion in the lattice, must be attributed to the delocalized nature of the electronic states and their strong mixing via the thermally occupied phonons in the initial state. This hypothesis could be indirectly verified, by observing that indeed the ionic states undergo shifts of ±0.1 eV for thermal samplings of nuclear coordinates. The fact that a single linewidth is used for all lines across the spectrum would indicate that the internal electronic states of the CN radical play a secondary role in the decay of the charge transfer states. Experimentally, fluorescence is only seen from the CN states. Given a radiative lifetime of $\sim 10^{-8}$ s for the ionic states (μ ~0.5 D, at 200 nm), assuming a fluorescence detection efficiency of 10^{-4}, we may conclude that the conversion to the CN internal electronic degrees of freedom must occur on a $t<1$ ps. Indeed, this must be an efficient channel to prevent the possibility of charge separation and trapping, which is observed in the case of halogen atom doped systems.[3] The latter process can be expected to occur via self-trapping of the hole, which must occur on the time scale of vibrational period of nearest neighbors of ~2 ps (based on the Debye frequency of the lattice). The conversion of the guest–hole charge transfer excitation to internal electronic excitation of the CN radical must occur on a time scale faster than 10^{-12} s to preclude self-trapping of the hole.

Given the accurate reproduction of the absorption spectrum in the extended solid, we may quantify the nature of the guest–host charge transfer states with some confidence. The clearest labeling of the observed states is the $J=3/2,1/2$ designation. By artificially increasing the spin–orbit coupling constant, it is verified that states contributing to absorption at $\lambda > 210$ nm belong to $J=3/2$ while states accessed at $\lambda < 210$ nm belong to $J=1/2$. This is consistent with the picture of a spin–orbit split valence band that is Coulombically bound to the ionic center—a picture reached from a very different starting point by von Grünberg and Gabriel.[11] Given the fact that the absorption edge is quantitatively reproduced, the shift between the predicted energy of the $S_{1/2}$-hole absorption and experiment may reflect a breakdown in the assumption of a constant value for the spin orbit splitting parameter, Δ. Beside this obvious feature, there clearly remains residual structure in each of the absorption bands, which is well reproduced by the simulation. However, as in the case of the smaller clusters, there is not a clear quantum label Ω (projection of total angular momentum) that can be associated with the observed substructure. In the standard model of a valence band hole, the clear separation between heavy and light bands ($\Omega=1/2,3/2$) is contingent upon a weak dependence of the spin–orbit interaction on the crystal momentum, $\hbar\mathbf{k}$, or equivalently, on the radial structure of the hole.[65] This assumption is no longer valid in guest–host charge transfer states, due to the strong Coulombic binding between ion and hole. It may be then expected that the spectral structure is related to the crystal momentum, which in turn should be reflected in the radial nodal structure of the hole. This is the picture implicit in the assignment of the substructure in halogen doped solids to a Rydberg hole progression.[10]

The extent of radial delocalization of the hole is perhaps the most distinctive characteristic of the guest–host charge transfer states and their dynamics. The hole density as a function of shell number is collected in Table I, for a representative set of states. Beside the spin–orbit splitting, the dominant factors that determine the structure and energetics

of the ionic states is the competition between hole delocalization and its Coulombic binding energy to the CN^- center. The delocalization energy can be quantified as the net exchange, $\langle J \rangle$, which can be computed from the eigenvector of a given state by nulling the pair exchange matrix (4),

$$\langle J \rangle_i = \langle i | \mathbf{H}(\mathbf{J}=0) | i \rangle - E_i . \tag{14}$$

The Coulombic binding energy, $\langle Q \rangle$, can be extracted in a similar fashion, or from the more transparent expression,

$$E(\text{Coulomb}) = \sum_i \delta(i) \cdot V_{\text{Kr}_i^+ \text{CN}^-}(r), \tag{15}$$

where $\delta(i)$ represents the hole density on the ith Kr atom. These quantities are also included in Table I.

The dissection presented by Table I is informative. The first five states, states 22–64, are representative of the clumps that carry most of the oscillator strength. The hole density in these states is predominantly on the first shell of nearest neighbors. It decreases monotonically as a function of energy of the ionic state, from 95% in state 22 to 68% in state 64. State 22 is representative of the intense first absorption band, while state 64 is the brightest single transition corresponding to the totally symmetric $S_{1/2}$-hole illustrated for $Kr_{12}CN$ in Fig. 9. In state 22, the radial density of the hole is oscillatory, it decreases to 0.1% on the second shell and grows back to 3% on the third shell and decays to zero by the fifth shell. In contrast, in the $S_{1/2}$-hole of state 64, the radial hole density decays monotonically without any nodal structure, with non-negligible amplitude of 0.5% out to the seventh shell, which is 10 Å removed from the CN center. There is a qualitative difference between the first five states and states 84–271, which carry significantly smaller transition dipoles. It can be verified that the drop in oscillator strength is a direct outcome of the drop in hole density on the first shell, therefore the drop in hole–electron overlap. Now, the exchange energy accounts for ~20% of the binding. The hole density in state 84 peaks on the third shell (38%). In state 131, which has significant transition dipole $\langle \mu \rangle^2 = 0.03$ D and contributes to the absorption wing of the $J = 1/2$ band, the hole density peaks on the third shell to a value of 58%. In state 194, which is a weak absorber ($\langle \mu \rangle^2 = 0.0046$ D), the radial density of the hole is oscillatory. It shows maxima on alternating on shells 3, 5, 7, and 9, with 10% of the density localized on shell 7, at $R = 10.6$ Å. Indeed, among the states that carry little transition dipole, e.g., states 221 and 271, the hole density can be significantly removed from the CN center. This trend continues with higher energy states, which however carry even smaller optical activity. The dark states can nevertheless couple to the optically accessible states via phonons, and therefore can act as effective channels for very fast charge delocalization. Any impurity that can act as an efficient hole trap can therefore be directly reached. This would explain the observation of H^+ centers in the IR spectra. However, experimentally, we do not observe a significant channel for charge separation via self-trapping. Evidently, the ionic states are efficiently coupled to the internal electronic states of the CN radical.

Finally, we do not find a clear label for the oscillatory structure in the $J = 3/2$ band, to associate it with the picture of a Rydberg progression.[10] The characteristics that would offer such a label would be the observation of a clear nodal structure in the radial density of the hole, with an increasing number of nodes as a function of energy. While state 22, which would be representative of the clump to be associated with the first state of such a progression has a node on the second shell; state 50, which would be the last clear member of the progression shows a monotonically decaying radial hole-density. Thus, it is not possible to identify the origin of the clumping of the states to hole momentum, neither is it possible to associate them with crystal field splittings of a common origin (angular momentum) since they are strongly mixed through spin–orbit interaction. The system seems intermediate between the various limits, as such, strongly mixed. It would be interesting to carry out a systematic analysis of the rare gas hosts, from Xe to Ne, to find the evolution of the good quantum numbers in such a series.

VII. CONCLUSIONS

The guest–host charge transfer states of CN doped Kr and Xe were observed experimentally, and were identified by direct analogy with those of the halogen doped solids. The spectrum could be simulated quantitatively in the extended DIIS formalism, using accurately determined pair parameters obtained from high level *ab initio* theory, and without further adjustment of parameters. This gives confidence to the method, and in particular to the treatment of transition dipoles, to the extent that the DIIS construct for such states can be expected to be predictive. With the inclusion of atomic hole functions distributed over 11 complete shells around the guest molecule, the presented real-space treatment bridges between the molecular and band limits. We have given a detailed dissection of structure and energetics of these states, because beyond the spin–orbit splitting into $J = 1/2$ and $J = 3/2$ bands, a simple classification does not seem to be applicable for these strongly mixed charge transfer states.

ACKNOWLEDGMENTS

This research was funded in part through a grant from the U.S. Air Force Office of Scientific Research (F49620-98-1-0163), a Fellowship provided by the Science Academy of Finland to one of the authors (J.E.) during his stay at Irvine. The experimental work, which was carried out in Jyväskylä, was funded by the Academy of Finland.

[1] M. E. Fajardo and V. A. Apkarian, J. Chem. Phys. **85**, 5660 (1986).
[2] M. E. Fajardo and V. A. Apkarian, J. Chem. Phys. **89**, 4102 (1988).
[3] M. E. Fajardo and V. A. Apkarian, J. Chem. Phys. **89**, 4124 (1988).
[4] H. Kunttu, J. Seetula, M. Rasanen, and V. A. Apkarian, J. Chem. Phys. **96**, 5630 (1992).
[5] H. Kunttu and J. A. Seetula, Chem. Phys. **189**, 273 (1994).
[6] M. Rasanen, J. Seetula, and H. Kunttu, J. Chem. Phys. **98**, 3914 (1993).
[7] G. Maier and C. Lautz, Angew. Chem. Int. Ed. Engl. **38**, 2038 (1999); G. Maier, D. Jurgen, R. Tross, H. P. Reisenauer, B. A. Hess, and L. J. Schaad, Chem. Phys. **189**, 383 (1994); G. Maier, H. P. Reisenauer, K. Lanz, R. Tross, D. Jurgen, B. A. Hess, and L. J. Schaad, Angew. Chem. Int. Ed. Engl. **32**, 74 (1993).
[8] I. Last and T. F. George, J. Chem. Phys. **87**, 1183 (1987).
[9] I. Last, T.-F. George, M. E. Fajardo, and V. A. Apkarian, J. Chem. Phys. **87**, 5917 (1987).

[10] N. Schwentner, M. E. Fajardo, and V. A. Apkarian, Chem. Phys. Lett. **154**, 237 (1989).
[11] H. H. von Grünberg and H. Gabriel, J. Chem. Phys. **105**, 4173 (1996).
[12] H. H. Von Grünberg, I. H. Gersonde, and H. Gabriel, Z. Phys. D: At., Mol. Clusters **28**, 145 (1993).
[13] M. Ovchinnikov and V. A. Apkarian, J. Chem. Phys. **110**, 9842 (1999).
[14] B. L. Grigorenko, A. V. Nemukhin, and V. A. Apkarian, J. Chem. Phys. **108**, 4413 (1998).
[15] F. Wittl and M. J. Creuzburg, J. Mol. Struct. **222**, 127 (1990); F. Wittl, J. Eberlein, T. Epple, M. Dechant, and M. J. Creuzburg, J. Chem. Phys. **98**, 9554 (1993).
[16] H. Kunz, J. G. McCaffrey, M. Chergui, R. Schriever, Ö. Ünal, V. Stepanenko, and N. Schwentner, J. Chem. Phys. **95**, 1466 (1991).
[17] J. Eloranta and H. Kunttu, J. Chem. Phys. **113**, 7446 (2000).
[18] H. Kunz, J. G. McCaffrey, M. Chergui, R. Schriever, Ö. Ünal, and N. Schwentner, J. Lumin. **48-49**, 621 (1991).
[19] S. Tanaka, H. Kajihara, S. Koda, and V. A. Apkarian, Chem. Phys. Lett. **233**, 555 (1995).
[20] M. S. Gudipati and M. Kalb, Chem. Phys. Lett. **307**, 27 (1999).
[21] J. Ahokas, K. Vaskonen, J. Eloranta, H. Kunttu, J. Phys. Chem. A **104**, 9506 (2000).
[22] A. D. Abbate and C. B. Moore, J. Chem. Phys. **82**, 1255 (1985).
[23] M. Pettersson, J. Lundell, L. Khriachtchev, and M. Räsänen, J. Chem. Phys. **109**, 618 (1998).
[24] H. Kunttu and J. Seetula, Chem. Phys. **189**, 273 (1994).
[25] G. Herzberg, *Spectra of Diatomic Molecules* (van Nostrand, New York, 1950).
[26] A. Thoma, G. Schallmoser, A. M. Smith, B. E. Wurfel, and V. E. Bondybey, J. Chem. Phys. **100**, 5387 (1994).
[27] V. E. Bondybey, J. Chem. Phys. **66**, 995 (1977).
[28] D. H. Katayama, T. A. Miller, and V. E. Bondybey, J. Chem. Phys. **71**, 1662 (1979).
[29] B. E. Wurfel, G. Schallmoser, G. M. Lask, J. Agreiter, A. Thoma, R. Schlachta, and V. E. Bondybey, Chem. Phys. **174**, 255 (1993).
[30] H. S. Lin, M. G. Erickson, Y. Lin, W. H. Basinger, W. G. Lawrence, and M. C. Heaven, Chem. Phys. **189**, 235 (1994).
[31] D. S. Tinti and G. W. Robinson, J. Chem. Phys. **49**, 3229 (1968).
[32] H. F. Schaefer III and T. G. Heil, J. Chem. Phys. **54**, 2573 (1971).
[33] S. E. Bradforth, E. H. Kim, D. W. Arnold and D. M. Neumark, J. Chem. Phys. **98**, 800 (1993).
[34] J. D. D. Martin and J. W. Hepburn, J. Chem. Phys. **109**, 8139 (1998).
[35] H. Kunttu, E. Sekreta, and V. A. Apkarian, J. Chem. Phys. **94**, 7819 (1991), and references therein.
[36] F. O. Ellison, J. Am. Chem. Soc. **85**, 3540 (1963).
[37] J. C. Tullu, Adv. Chem. Phys. **42**, 63 (1980); J. C. Tully, in *Modern Theoretical Chemistry*, edited by G. A. Segal (Plenum, New York, 1976).
[38] P. J. Kuntz, in *Theoretical Models of Chemical Bonding*, edited by Z. B. Maksic (Springer, Berlin, 1990).
[39] E. L. Pollock and B. J. Alder, Phys. Rev. Lett. **41**, 903 (1978).
[40] E. S. Rittner, J. Chem. Phys. **19**, 1030 (1951).
[41] H. Frohlich, *Theory of Dielectrics* (Oxford, London, 1949), Vol. II.
[42] F. Mies, Phys. Rev. A **7**, 942 (1973).
[43] F. Y. Naumkin, Chem. Phys. **252**, 301 (2000).
[44] F. X. Gadea and M. Amarouche, Chem. Phys. **140**, 385 (1990).
[45] A. Bastida and F. X. Gadea, Chem. Phys. **209**, 291 (1996).
[46] For the angular anisotropy of the ground state potentials see the related system of CN–Ne in M. Yang and M. H. Alexander, J. Chem. Phys. **107**, 7148 (1997); W. G. Lawrence, Y. Chen, and M. C. Heaven, *ibid.* **107**, 7163 (1997); M. C. Heaven, Y. Chen, and W. G. Lawrence, in *Advances in Molecular Vibrations and Collision Dynamics*, (JAI, New York, 1998), Vol. 3, pp. 91–126.
[47] G. Schallmoser, A. Thoma, B. E. Wurfel, and V. E. Bondybey, Chem. Phys. Lett. **219**, 101 (1994).
[48] R. A. Aziz and M. J. Slaman, Mol. Phys. **58**, 697 (1986).
[49] K. Raghavachari, G. W. Trucks, J. A. Pople, and M. Head-Gordon, Chem. Phys. Lett. **157**, 479 (1989); P. J. Knowles, C. Hampel, and H. J. Werner, J. Chem. Phys. **99**, 5219 (1993); C. Hampel, K. Peterson, and H. J. Werner, Chem. Phys. Lett. **190**, 1 (1992).
[50] T. H. Dunning, Jr., J. Chem. Phys. **90**, 1007 (1989); R. A. Kendall, T. H. Dunning, Jr., and R. J. Harrison, *ibid.* **96**, 6769 (1992).
[51] A. Nicklass, M. Dolg, H. Stoll, and H. Preuss, J. Chem. Phys. **102**, 8942 (1995).
[52] T. J. Lee and P. R. Taylor, Int. J. Quantum Chem. **23**, 4936 (1989).
[53] F. Boys and F. Bernardi, Mol. Phys. **19**, 553 (1970).
[54] P. J. Knowles and H.-J. Werner, Chem. Phys. Lett. **115**, 259 (1985), H.-J. Werner and P. J. Knowles, J. Chem. Phys. **82**, 5053 (1985).
[55] H.-J. Werner and P. J. Knowles, J. Chem. Phys. **89**, 5803 (1988); P. J. Knowles and H.-J. Werner, Chem. Phys. Lett. **145**, 514 (1988); Theor. Chim. Acta **84**, 95 (1992).
[56] M. R. A. Blomberg and P. E. M. Siegbahn, J. Chem. Phys. **78**, 5682 (1983); S. R. Langhoff and E. R. Davidson, Int. J. Quantum Chem. **8**, 61 (1974).
[57] A. Berning, H.-J. Werner, P. Palmieri, and P. J. Knowles (unpublished results).
[58] (a) MOLPRO is a package of *ab initio* programs written by H.-J. Werner, and P. J. Knowles, with contribution from R. D. Amos, A. Bernhardsson, A. Bering *et al.*, (b) F. Eckert, P. Pulay, and H. J. Werner, J. Comput. Chem. **18**, 1473 (1997).
[59] H. Kunttu, J. Feld, R. Alimi, A. Becker, and V. A. Apkarian, J. Chem. Phys. **92**, 4856 (1990).
[60] R. Signorell, U. Hollenstein, and F. Merkt, J. Chem. Phys. **114**, 9840 (2001).
[61] R. B. Jones, H. C. Tran, and J. G. Eden, J. Chem. Phys. **102**, 4329 (1995).
[62] L. C. Lee, G. P. Smith, T. M. Miller, and P. C. Cosby, Phys. Rev. A **17**, 2005 (1978).
[63] Tabulations and detailed tests of the potentials used can be found in S. L. Fieldler, Ph.D. thesis, UCI, 2002.
[64] Z. Y. Chen, C. D. Cogley, J. H. Hendricks, B. D. May, and A. W. Castleman, Jr., J. Chem. Phys. **93**, 3215 (1990).
[65] J. M. Luttinger and W. Kohn, Phys. Rev. **97**, 869 (1955).